
1 **Dynamic Response of Pile-Slab Retaining Wall Structure**
2 **under Rockfall Impact**

3 Peng Zou^{1,2,3}, Gang Luo^{1,*}, Yuzhang Bi⁴, Hanhua Xu^{2,3}

4 1. *Faculty of Geosciences and Engineering, Southwest Jiaotong University, Chengdu 611756,*
5 *China*

6 2. *Kunming Prospecting Design Institute of China Nonferrous Metals Industry Co., Ltd, Yunnan*
7 *650051, China*

8 3. *Yunnan Key Laboratory of Geotechnical Engineering and Geohazards, Kunming, 650051,*
9 *China*

10 4. *College of Resources and Environment, Fujian Agriculture and Forestry University, Fuzhou*
11 *350002, China*

12 ***Corresponding author at:** Faculty of Geosciences and Engineering, Southwest Jiaotong
13 University, Chengdu 611756, China

14 E-mail addresses: luogang@home.swjtu.edu.cn (G. Luo).

15 **Abstract:** The pile-slab retaining wall, as an innovative rockfall protection structure, has been
16 extensively utilized in the western mountainous regions of China. With its characteristics of a
17 small footprint, high interception height, and ease of construction, this structure demonstrates
18 promising potential for application in mountainous regions worldwide, such as the Himalayas,
19 Andes, and Alps. However, its dynamic response upon impact and impact resistance energy
20 remain ambiguous, due to the intricate composite nature of the structure. To elucidate this, an
21 exhaustive dynamic analysis of a four-span pile-slab retaining wall with a cantilever section of 6
22 m under various impact scenarios was conducted utilizing the finite element numerical simulation
23 method. The rationality of the selected material constitutive models and the numerical algorithm
24 was validated by reproducing two physical model tests. The simulation results reveal the
25 following: (1) The lateral displacement of the pile at the ground surface and the concrete damage
26 under the pile as the impact center is greater than those under the slab as the impact center,
27 implying that the impact location has a significant influence on the stability of the structure. (2)
28 There is a positive correlation between the response indexes (impact force, interaction force,
29 lateral deformation of pile and slab, concrete damage) and the impact velocities. (3) The rockfall
30 peak impact force, the ratio of peak impact force to peak interaction force, and lateral
31 displacement of pile at the ground surface had strong linear relationships with rockfall energy. (4)
32 Relative to the bending moment, shear force and damage degree, the lateral displacement of pile at
33 the ground surface is the first to reach its limit value. Taking the lateral displacement of the pile at
34 the ground surface as the controlling factor, the estimated maximum impact energy that the pile-
35 slab retaining wall can withstand is 905 kJ in this study when the structure top is taken as the
36 impact point. In cases where the impact energy of falling rocks exceeds 905 kJ, it is recommended
37 to optimize the mechanical properties of the cushion layer, improve the elastic modulus of
38 concrete, increase the reinforcement ratio of longitudinal tension bars, enlarge the section size of
39 pile at ground level, or add anchoring measures to enhance the bending resistance of the retaining
40 structure.

41 **Keywords:** rockfall, pile-slab retaining wall, numerical simulation, dynamic response

42 List of symbols

P	Actual lateral soil resistance (kPa).	F_{dm}	Peak impact force (kN).
P_u	Ultimate lateral soil resistance (kPa).	F_{im}	Peak interaction force (kN).
$S_{u_{cu}}$	Consolidated isotropic undrained tri-axial shear strength of soil (kPa/m).	α	Ratio of the peak impact force to the peak interaction force (%).
y	Actual lateral soil deformation (m).	S_{mpt}	Maximum lateral displacement of pile at the ground surface (mm).
B	Pile width (m).	N_d	Number of damage failure units.
z	Depth below the ground surface (m).	β	Ratio of damage failure units to overall structure units (%).
S_p	Shape correction factor of pile section.	m	Impactor mass (kg).
E	Initial kinetic energy of impactor.	v	Initial velocity of impactor (m/s).

43 1. Introduction

44 Rockfall disasters pose a great threat to roads, railways, buildings and inhabitants in
45 mountainous terrain (Hung et al., 2014; Crosta and Agliardi, 2004; Shen et al., 2019). It can be
46 described as a process that the rapid bouncing, rolling and sliding movement of one (or several)
47 boulders down a slope (Peila and Ronco, 2009). Muraishi et al. (2005) surveyed 607 rockfall
48 events and found that about 68% of rockfall events have an impact energy of less than 100 kJ,
49 whereas 90% have less than 1000 kJ. Chau et al. (2002) indicated that the rotational kinetic energy
50 of rockfall only accounts for 10% of the total kinetic energy. To mitigate such geological hazards,
51 scholars and engineers have proposed different types of technical solutions. Two primary
52 categories of defensive measures are commonly employed: active and passive. Active protection
53 measures mainly include masonry protection, reinforcement protection (grouting, anchor rod, and
54 anchor cable), initiative protective net (Yang et al., 2019). Passive protection measures include
55 passive flexible protection (Yu et al., 2021), rockfall shed gallery (Zhao et al., 2018), rockfall
56 retaining wall. Considering many factors, such as technological feasibility and economic
57 considerations, rockfall retaining wall is frequently employed in practical engineering (Volkwein
58 et al., 2011).

59 Currently, various types of retaining walls are utilized in engineering projects aimed at
60 intercepting falling boulders. These include masonry retaining walls, reinforced concrete (RC)
61 retaining walls, reinforced soil retaining walls, and pile-slab retaining walls (PSRW). Due to

62 inherent structural weakness of these walls, their ability to absorb the impact energy from rockfall
63 is limited (Mavrouli et al., 2017). To enhance the impact resistance, the reinforced concrete
64 retaining walls have been utilized (Yong et al., 2020). These structures can intercept rockfall
65 impact energy ranging approximately from 120 to 500 kJ (Maegawa et al., 2011). To prevent
66 concrete from being damaged by the direct impact of rockfall, a buffer layer is generally added in
67 front of the structure for protection, such as reinforced soil and gabion cushion (Perera et al.,
68 2021). Although the impact resistance of the structure has been improved, there is still a problem
69 of limited interception height. When the required interception height is large, the foundation size
70 has to be increased to prevent the structures from overturning. In order to mitigate against rockfall
71 events involving higher energy levels, numerous researchers have proposed the implementation of
72 reinforced soil retaining walls. Extensive studies have been conducted in this regard,
73 demonstrating that the structures can effectively intercept rockfall impact energies exceeding 5000
74 kJ (Lambert et al., 2009). Moreover, geosynthetic have proven to be efficacious in reducing wall
75 stresses (Lu et al., 2021). However, the structure requires a substantial spatial footprint and poses
76 an overturning risk during construction in steep terrain (Peila et al., 2007). Additionally, when the
77 topography at the wall site features steep slopes, the available space behind the wall for
78 accommodating rockfalls becomes constrained.

79 In response to the challenges posed by steep terrains, narrow site conditions, and suboptimal
80 foundation conditions in mountainous terrain, Hu et al. (2019) introduced the PSRW structure.
81 The structures are composed of a buffer layer and an anti-slid pile-slab structure, which has found
82 widespread application in southwestern China (Fig. 1). Due to its implementation of pile
83 foundations, this structure possesses characteristics such as a small footprint, high interception
84 height, and ease of construction. However, the current PSRW design verification is to treat the
85 structure as an underground continuous wall (CAGHP, 2019). And, due to the composite nature of
86 this structure, the dynamical response at various impact points remains ambiguous. The maximum
87 impact energy that the structure can withstand has also not been thoroughly investigated. It can
88 lead to potential underestimation of failure possibilities (Fig. 1d). At the same time, the existing
89 research focuses on the single slab and pile impacted by rockfall (Wu et al., 2021; Yong et al.,
90 2021).



Fig. 1. PSRW in south-western China (a) Kongyu town (b) Jiuzhaigou nature reserve (c) Zhenjiangguan tunnel exit in Chengdu-lanzhou railway (d) Wenchuan-Maerkang expressway.

91 Therefore, analysis of structural dynamic response and concrete damage is crucial to
 92 determine its effectiveness in mitigating rockfall hazards. Based on the unique advantages of the
 93 finite element method, this study employs the LS-DYNA to simulate the complete process of
 94 rockfall impacting on PSRW. This methodology has been widely adopted by numerous researchers
 95 and demonstrated as suitable for simulating impact problems of reinforced concrete structure
 96 (Zhong et al., 2022; Fan et al., 2022; Bi et al., 2023). In conclusion, a full-scale numerical model
 97 of a four-span pile-slab retaining wall satisfying specification requirements is established. The
 98 rationality of the selected material constitutive models and a numerical algorithm was validated by
 99 reproducing two physical model tests. The structure's dynamic behavior under different impact
 100 velocities and impact centers is discussed (Fig. 2). The results provide insights into structure
 101 dynamic response analysis of the PSRW and serve as a benchmark for further research.

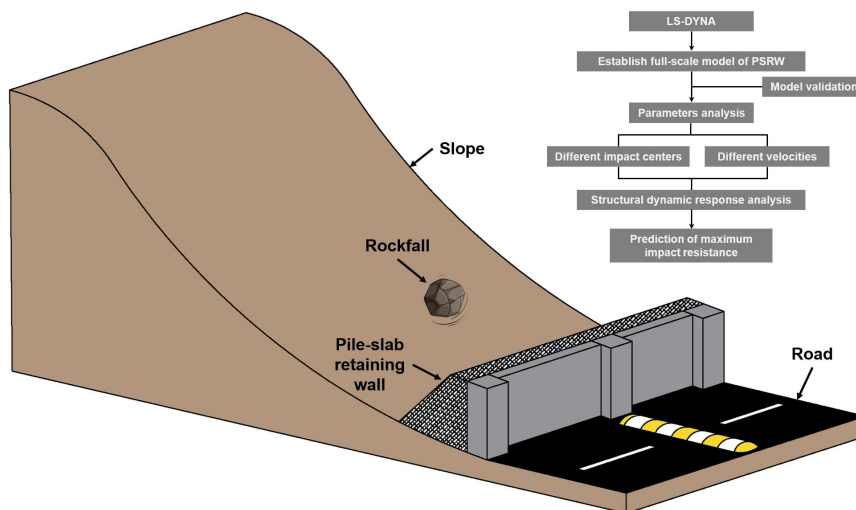


Fig. 2 Mind mapping.

102 2. Numerical model and validations

103 2.1. Model configuration

104 2.1.1. Engineering background

105 The design drawing of the PSRW (Fig. 3) is consistent with the actual project located in
106 Zhangmu Town, China. Given the large scale of the actual engineering structure, numerical
107 simulations have been focused solely on a representative four-span structure, incorporating
108 appropriately simplified boundary conditions to facilitate the analysis. For a comprehensive
109 understanding of the modeling specifics, kindly refer to Section 2.1.3. The anti-slide piles with a
110 concrete protective layer thickness of 0.04 m have a cross-section area of 1.8 m × 1.25 m. The
111 total pile length is 12 m, and the embedded section is 6 m. The HRB 400 longitudinal bar with
112 diameters of 25 mm and 32 mm were arranged in the pile (Fig. 3c). The stirrups are HRB335 with
113 a diameter of 16 mm and a spacing of 200 mm. The slabs between the piles are 6 m in length, 3.5
114 m in width, and 0.5 m in thickness. These slabs contain two layers of 16 mm-diameter reinforced
115 bar. The sand buffer layer are 1 m and 5 m on top and bottom, respectively. A geogrid is
116 horizontally placed in the buffer layer at 0.25 m intervals. Lastly, 1 m³ sphere rock boulder with a
117 diameter of 1.24 m was set as an impactor. The impact locations are 2# slab center (CS) and 3#
118 pile center (CP) at 5.25 m over the ground.

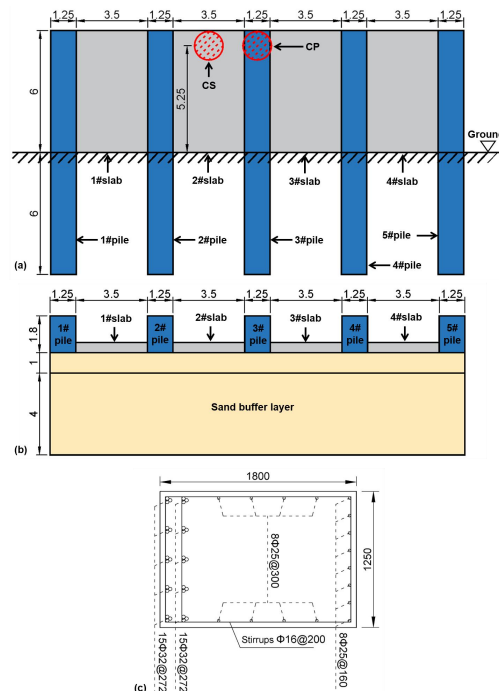


Fig. 3. The design diagram of PSRW (a) front view (unit: m) (b) top view (unit: m) (c) cross-section profile of pile (unit: mm).

119 2.1.2. *Soil-pile interaction*

120 Under the impacting, the lateral deformations of the pile are greatly influenced by the plastic
121 behavior of the soil, particularly the soil near the pile. Given their importance and complexity, it
122 isn't easy to thoroughly describe soil-pile interactions. This paper calculates the pile-soil
123 interaction by the lateral resistance-deflection (p - y) curve method. As state by Truong and Lehane
124 (2018), the p - y curves for square cross-section pile are utilized as

125
$$\frac{P}{P_u} = \tanh \left[5.45 \left(\frac{y}{B} \right)^{0.52} \right] \quad (1)$$

126
$$\frac{P}{S_{u_cu}} = 10.5 \left[1 - 0.75 e^{-0.6z/B} \right] S_p \quad (2)$$

127 where P is the actual lateral soil resistance, kPa; P_u is the ultimate lateral soil resistance, kPa;
128 S_{u_cu} is consolidated isotropic undrained triaxial shear strength of soil, kPa/m; y is the actual lateral
129 soil deformation, m; B is pile width, m; z is depth below the soil surface, m; S_p is a shape
130 correction factor.

131 According to the reference and simulated model, the S_{u_cu} and S_p are adopted as 1.5 kPa/m
132 and 1.25, respectively. Besides, the soil is modeled by compressive inelastic springs, arranged
133 every 0.25 m along the pile height and side (Fig. 4a).

134 2.1.3. *Numerical model and numerical simulation scheme*

135 (1) Numerical model

136 The numerical model of PSRW is shown in Fig. 4. The material constitutive models, unit
137 types, physical-mechanical parameters, and parameter source for all components are listed in
138 Table 1. The rationality of all material constitutive models and physical mechanics parameters
139 were verified in Section 2.2. The bottom of piles and buffer layers are fixed for the boundary
140 conditions. Additionally, both sides of the buffer layer are blocked by infinitely rigid walls. The
141 contact type between the rockfall, sand buffer layer, and pile-slab structure was set to automatic
142 surface-to-surface.

143 (2) Numerical simulation scheme

144 According to previous research (Muraishi et al., 2005; Chau et al., 2002), angular velocity of

145 impactor was neglected in numerical simulations, and line velocities were set as 10, 15, 20, 25,
 146 and 30 m/s, corresponding to impact energies of 130, 292.5, 520, 812.5, and 1170 kJ (Table 2).
 147 The linear velocity is perpendicular to surface of the buffer layer.

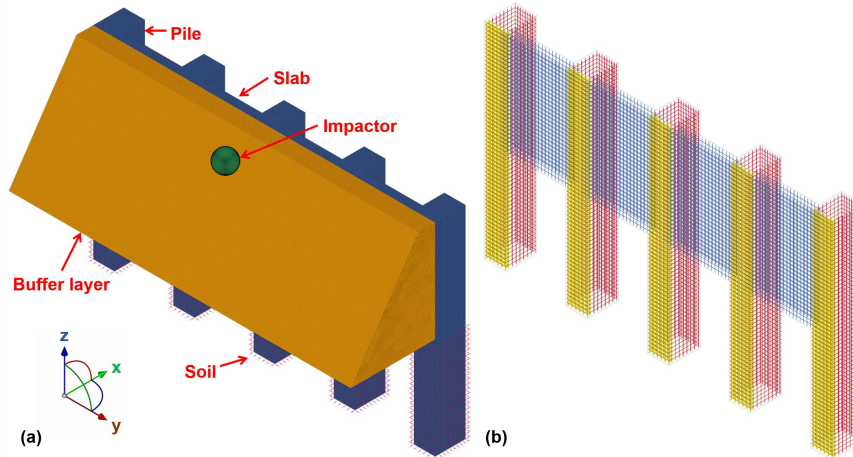


Fig. 4. Numerical model of the PSRW (a) numerical model (b) reinforced bar of PSRW (unit: mm).

148 **Table 1** Material constitutive model and physical-mechanical parameters for various components of PSRW.

Items	Constrained model	Unit types	Integral methods	Density (kg/m ³)	Young's modul (MPa)	Poisson's ratio
Concrete	Continue cap concrete (MAT_159) (Heng et al., 2021)	Solid element	One integration point	2450	30000	0.3
Reinforced bar	Plastic kinematic model (MAT_003) (Heng et al., 2021)	Beam element	2×2 Gauss integration	7850	204000	0.3
Sand buffer layer	Soil-foam model (MAT_063) (Bhatti and Kishi, 2010)	Solid element	One integration point	1720	100	0.3
Impactor	Rigid body (MAT_020)	Solid element	One integration point	2600	20000	0.25
Geogrid	Plastic kinematic model (MAT_003) (Lee et al., 2010)	Shell element	Belytschko-Tsay integration	1030	464	0.3

149 **Table 2** Detailed numerical simulation scheme.

Case	Impact location	Impact height (m)	Impact velocity (m/s)	Impact kinetic energy (kJ)
CP-V10	3# pile center	5.25	10	130
CP-V15			15	292.5
CP-V20			20	520
CP-V25			25	812.5
CP-V30			30	1170
CS-V10	2# slab center	5.25	10	130
CS-V15			15	292.5
CS-V20			20	520
CS-V25			25	812.5
CS-V30			30	1170

150 Note: CP denotes the 3# pile center as impact location; CP denotes the 2# slab center as impact location; V denotes
 151 the velocities of rockfall.

152 2.2. Model validation

153 In order to verify the rationality of the selected material constitutive model and the
 154 established numerical model. Two physical model tests from previously published papers (Heng et

155 al., 2021; Demartino et al., 2017; Schellenberg, 2008) were selected to reproduce.

156 *2.2.1. Failure test of RC cantilever column*

157 The physical model test conducted by Demartino et al. (2017) was selected to verify the
158 ability of constitutive model to reflect the accumulative damage for RC structures under impact
159 loads. The model is composed of a cylindrical column with a diameter of 0.3 m and a height of 1.7
160 m, and a square-section concrete foundation with length of 0.9 m and height of 0.5 m. The column
161 was reinforced with sixteen 8 mm diameter longitudinal reinforced bar and 6.5 mm diameter
162 stirrups at 100 mm spacing. The foundation was firmly connected to the ground using four 50 mm
163 diameter high-strength prestressed reinforced bar. The experiment involved a test truck made of
164 Q235 steel (considered as a rigid body) (Fig. 5a). The impactor was positioned 0.4 m above the
165 bottom of the column and was released at a velocity of 3.02 m/s (impact energy of 7.21 kJ). Fig.
166 5b shows the numerical model with hexahedral mesh. The material constitutive models for
167 components are shown in Table 1. For the boundary conditions, the model was fixed with four
168 high-strength bolts.

169 The trend and amplitude of the impact forces by numerical simulations closely matched the
170 experimental results (Fig. 6). Similarly, Table 3 Simulation results of different mesh sizes.

Items	Impact force (kN)	Displacement of column at 1.2m height (mm)	Number of the element	Computational time (hour)
Physical model test	999.52	22.3	/	/
25 mm mesh size	966.72	23.1	5462900	24
50 mm mesh size	978.1	22	807534	4.2
100 mm mesh size	1009.35	21.3	172268	1.2

171 **Table 4** indicates a consistency between the extent of the experimental and numerical
172 damage in concrete. The deviations of peak impact forces between the numerical simulations and
173 the experiments were below 10% (Table 3). These results suggest that the numerical model and its
174 governing parameters can reliably simulate the accumulative damage in RC structures subjected to
175 impact loads. Considering both accuracy and computational time, a mesh size of 50 mm was
176 selected for the numerical simulations conducted in this study.

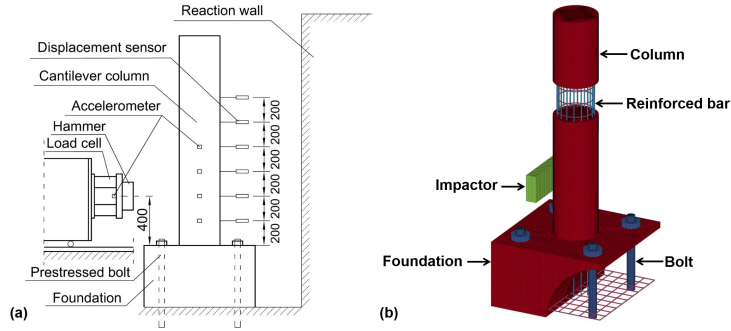


Fig. 5. Model of RC cantilever column failure test (a) experimental model (b) numerical model (unit: mm).

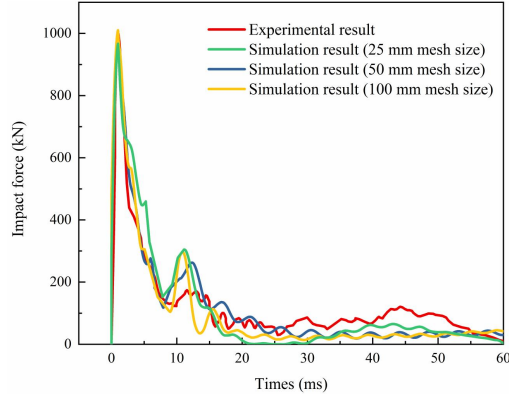


Fig. 6. Dynamic curve of impact force with different mesh size.

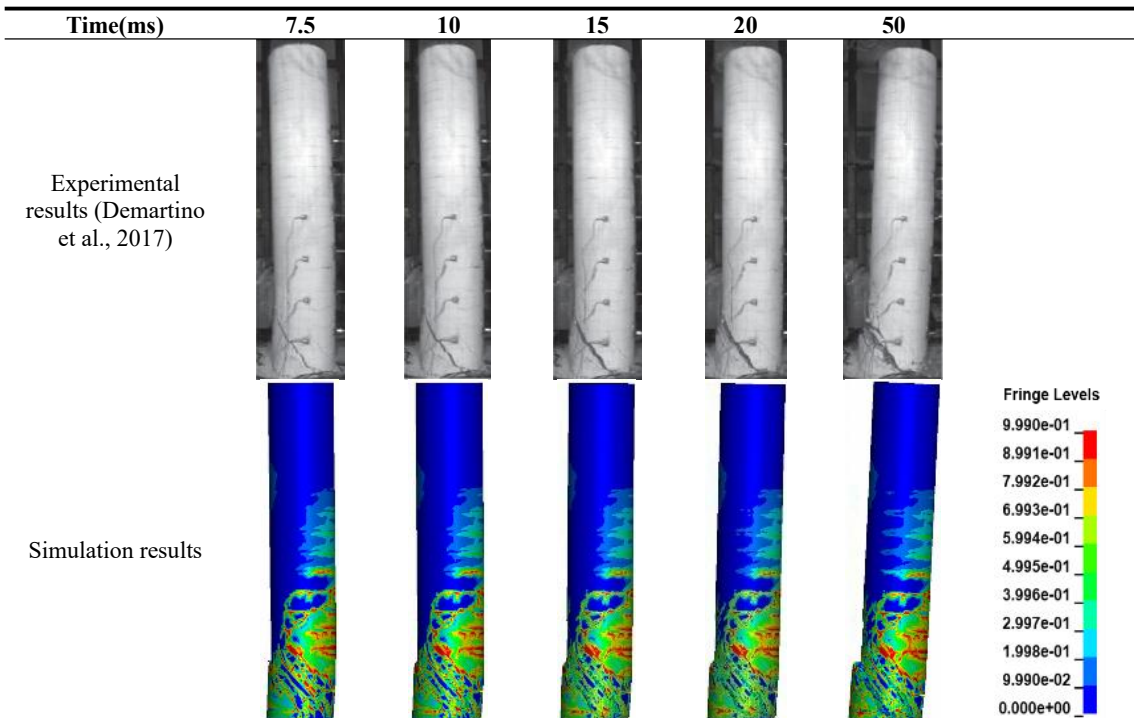
177

Table 3 Simulation results of different mesh sizes.

Items	Impact force (kN)	Displacement of column at 1.2m height (mm)	Number of the element	Computational time (hour)
Physical model test	999.52	22.3	/	/
25 mm mesh size	966.72	23.1	5462900	24
50 mm mesh size	978.1	22	807534	4.2
100 mm mesh size	1009.35	21.3	172268	1.2

178

Table 4 Comparison of experimental and simulation results of concrete damage accumulation with time.



179 2.2.2. Failure test of RC slab with a buffer layer

180 The physical model test conducted by Schellenberg (2008) was selected to validate the
 181 capability of the constitutive model to reflect the interaction among the boulder, sand buffer layer,
 182 and RC structure. The specimen comprises a RC slab measuring $1.5\text{ m} \times 1.5\text{ m} \times 0.23\text{ m}$ and a
 183 sand buffer layer with 0.5 m in radius and 0.45 m in thickness (Fig. 7). The slab is reinforced with
 184 one layer of reinforced bar with 12 mm diameter and a spacing of 95 mm for the lower layer. The
 185 diameter and density of the boulder are 0.8 m and 3110 kg/m^3 , respectively. The impact position is
 186 located at the center of the buffer layer, with an impact velocity of 5.5 m/s (impact energy of 14.4
 187 kJ). The material constitutive models for concrete, reinforced bar, and sand buffer layer are shown
 188 in Table 1. For the boundary conditions, the bottom of the supports was fixed.

189 Fig. 8 presents the dynamic curve of impact force, displacement of slab center, and axial
 190 strain of center reinforced bar. The results demonstrate that the deviations of the peak impact force,
 191 the maximum strain of reinforced bar, and the slab center displacement are less than 10% .
 192 Therefore, the numerical model and its governing parameters are deemed reliable for simulating
 193 the behavior of a sand cushion layer and an RC structure under impact loads.

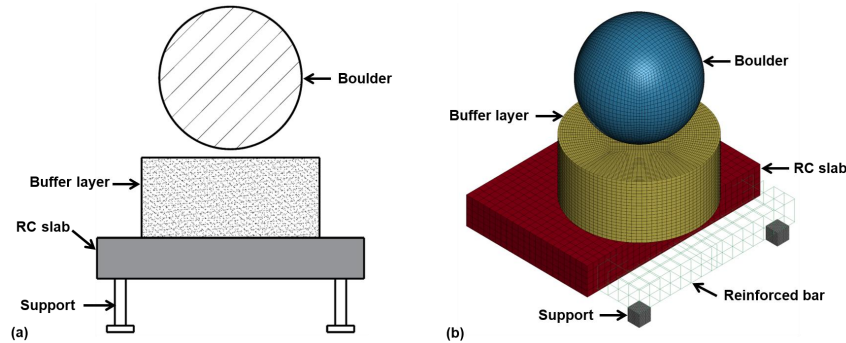
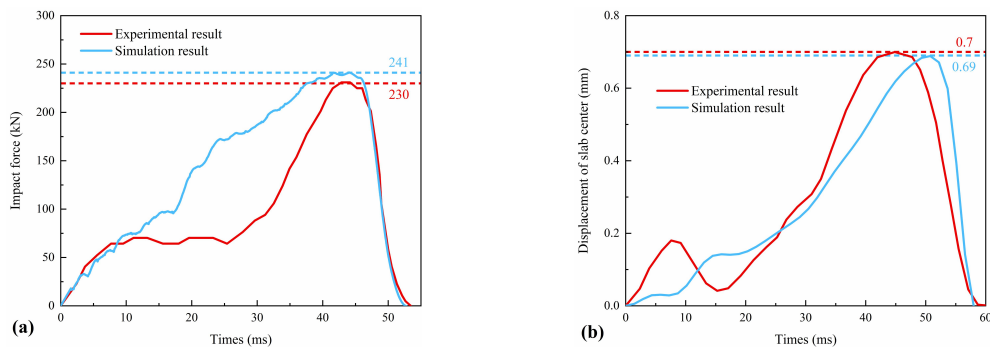


Fig. 7. Model of RC slab failure test
 (a) experimental model (b) numerical model (unit: mm).



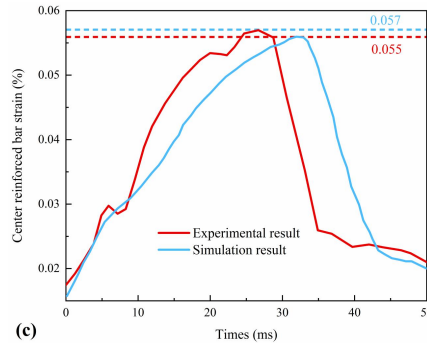


Fig. 8. Comparisons between experimental and simulation results
(a) impact force (b) displacement of slab center (c) axial strain of reinforced bar.

194 3. Numerical results

195 In this section, the dynamic response of PSRW under different impact centers and different
196 impact velocities are compared and analyzed. The main evaluation indexes are as follows: impact
197 force (the contact force between the impactor and the buffer layer), interaction force (the contact
198 force between the buffer layer and the RC structure), stress of concrete and reinforced bar,
199 concrete damage, lateral displacement at the crown of different components (piles and slabs), and
200 lateral displacement of all piles at the ground surface.

201 3.1. Influence of different impact centers

202 To analyze the influence of dynamic behaviors of PSRW under different impact centers, two
203 group simulations under maximum impact energy (CP-V30 and CS-V30) are selected for
204 comparison.

205 3.1.1. Impact force and interaction force

206 Fig. 9a and 9b show the dynamic curves of the impact force and interaction force,
207 respectively. Both force curves exhibit a distinct single-peaked pattern. The impact force rapidly
208 reduces to zero due to the energy-dissipating properties of the sand buffer layer (Fig. 9a). In
209 contrast, the interaction force remains at a non-zero value (475 kN) (Fig. 9b). Owing to the
210 permanent deformation sustained by the structure, and the gravitational force exerted by the sand
211 buffer acts on the surface of the structure. Furthermore, Fig. 9a illustrates the close overlap of the
212 impact forces for various impact centers, depending on the buffer and impactor characteristics, and
213 minimally affected by the impact center. The slight differences observed in the dynamic curve of
214 interaction force under CP-V30 and CS-V30 may be attributed to the flexural stiffness of the slab
215 and pile.

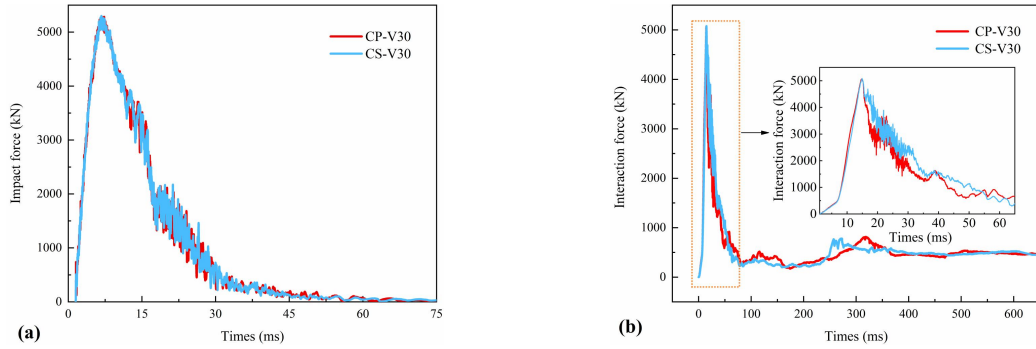
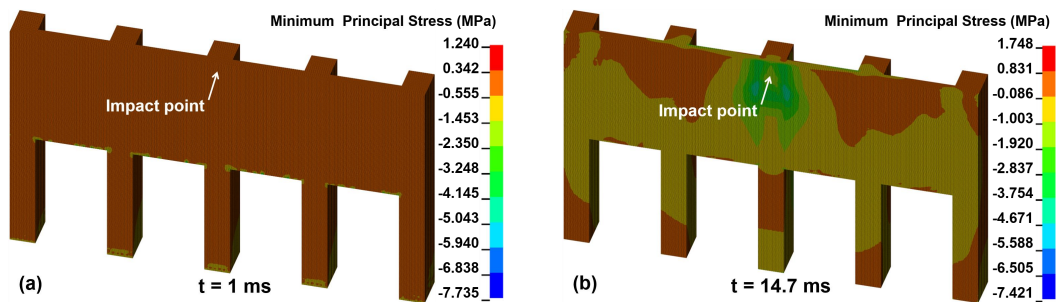


Fig. 9. Dynamic curves of impact force and interaction force under various impact centers
 (a) impact force (b) interactional force.

216 3.1.2. *Stress of concrete*

217 The minimum principal stress of concrete and the effective stress of reinforced bar are
 218 important indexes to evaluate the dynamic response of RC structures (Zhong et al., 2021; Zhong et
 219 al., 2022). Fig. 10 shows the minimum principal stress nephogram of concrete under CP-V30 from
 220 1 to 650 ms. When $t = 1$ ms (Fig. 10a), the minimum stress focus on the bottom of the piles. When
 221 $t = 14.7$ ms (Fig. 10b), the minimum principal stress of concrete around the impact point increased
 222 rapidly to 7.421 MPa. When $t = 22.8$ ms (Fig. 10c), the concrete elements at the joints of the 3#
 223 pile and slabs achieve compressive strength, leading to concrete damage. When $t = 650$ ms (Fig.
 224 10d), the total volume of damaged elements reaches 0.63 m^3 , which occupies a proportion of
 225 0.35%.

226 Fig. 11 shows the minimum principal stress nephogram of concrete under CP-V30 from 1 to
 227 650 ms. When $t = 1$ ms, the maximum stress focus on the bottom of the piles (Fig. 11a). When $t =$
 228 14.7 ms, the minimum principal stress around the impact point increased rapidly to 12.117 MPa
 229 (Fig. 11b). When $t = 22.4$ ms, the elements of the concrete at the impact point of the 2# slab
 230 achieve ultimate compressive strength, leading to the concrete damage (Fig. 11c). When $t = 650$
 231 ms, the total volume of damage elements reaches 0.61 m^3 (Fig. 11d), which occupies a proportion
 232 of 0.34%.



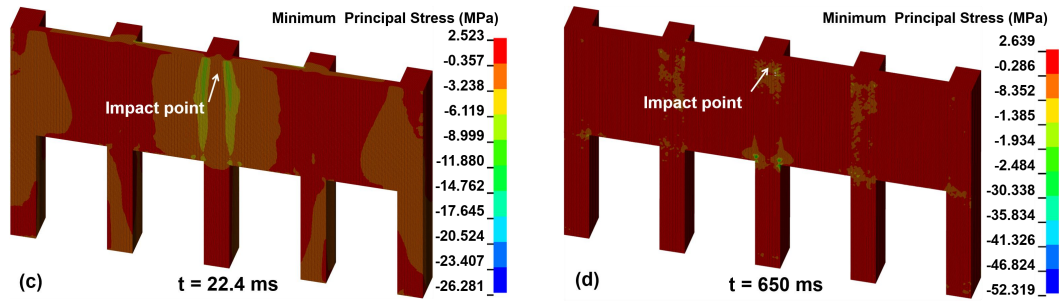


Fig. 10. Minimum principal stress nephogram of concrete under CP-V30.

233

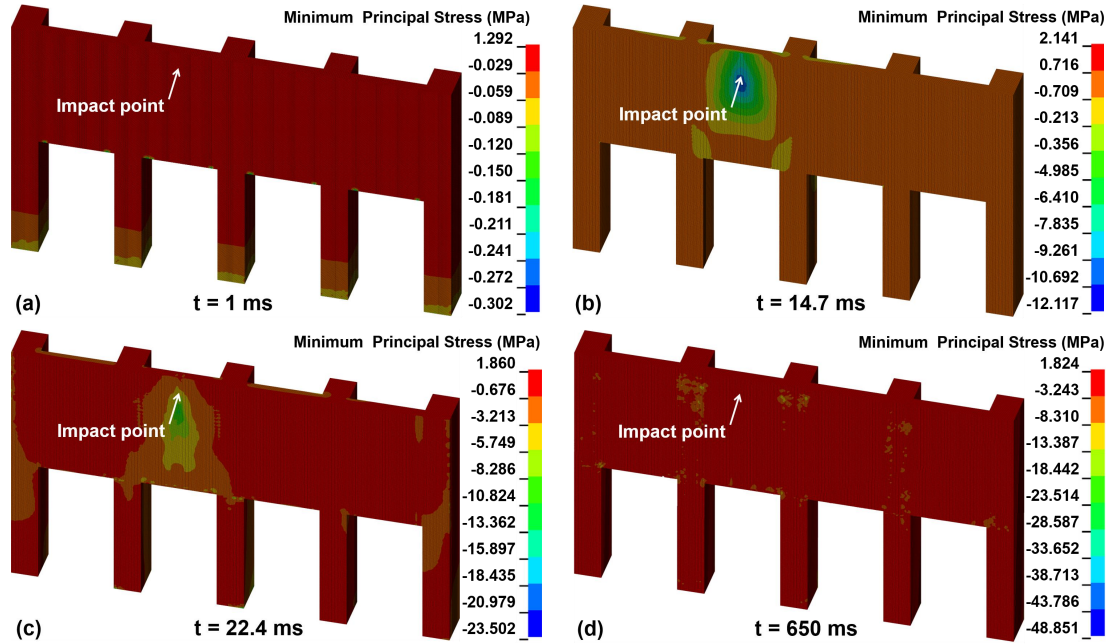


Fig. 11. Minimum principal stress nephogram of concrete under CS-V30.

234 3.1.3. Stress of reinforced bar

235 Fig. 12 shows the effective stress nephogram of the reinforced bar from 1 to 650 ms under
 236 the condition of CP-V30. It can be observed that: (i) when $t = 1$ ms, the maximum stress
 237 concentrated at the bottom of the pile (Fig. 12a); (ii) when $t = 14.7$ ms (the moment of attaining
 238 the maximum interaction force), the maximum stress concentrated at the vicinity of the impact
 239 point and the joints of piles and slabs (Fig. 12c); (iii) when $t = 650$ ms, the maximum stress
 240 concentrated at the longitudinal bar of 2#, 3#, and 4# pile (Fig. 12d). Noteworthily, the effective
 241 stress of reinforced bar did not exceed the ultimate yield stress.

242 Fig. 13 shows the effective stress nephogram of reinforced bar from 1 to 650 ms under CS-
 243 V30. It can be observed that: (i) when $t = 1$ ms, the maximum stress concentrated at the bottom of
 244 the pile (Fig. 13a); (ii) when $t = 14.7$ ms, the effective stress of reinforced bar around the impact
 245 point increased rapidly to 137.2 MPa (Fig. 13c); (iii) when $t = 650$ ms, the maximum stress

concentrated at the longitudinal bar of 2#, 3#, and 4# pile (Fig. 13d). Noteworthy, the effective

stress of reinforced bar did not exceed the ultimate yield stress.

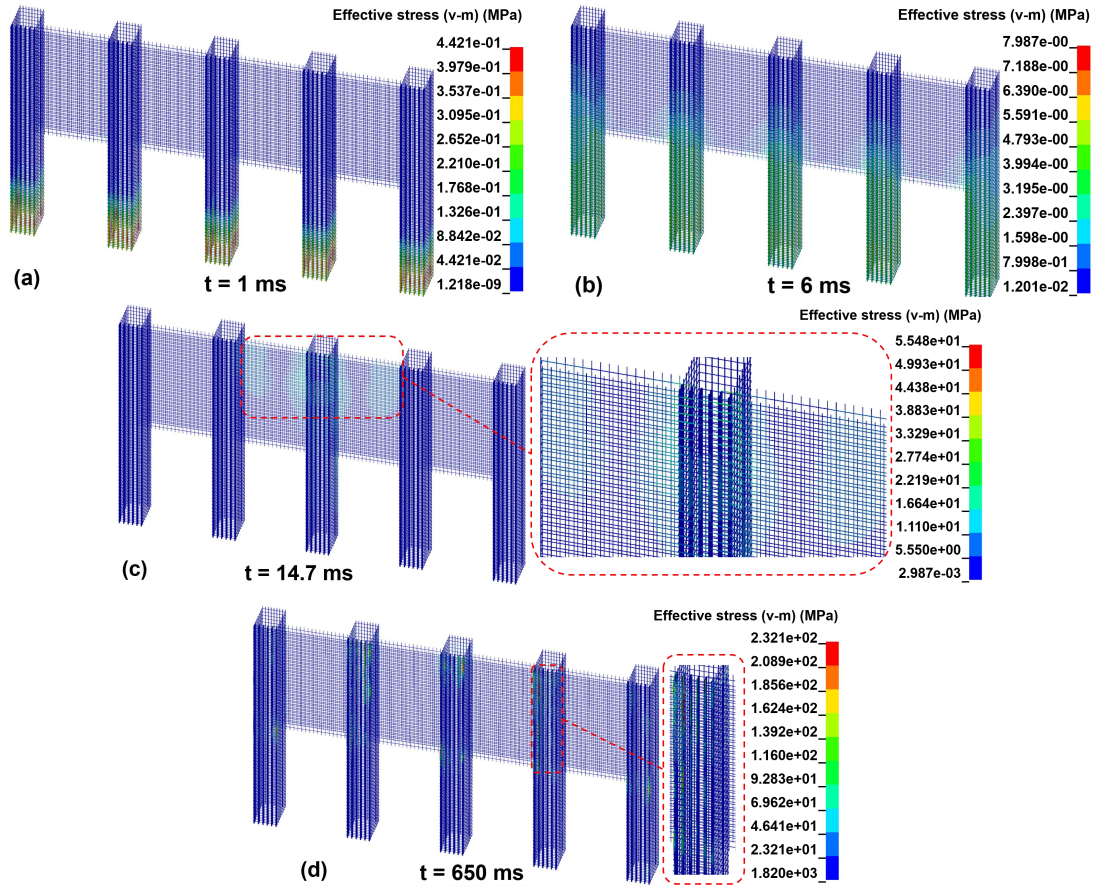
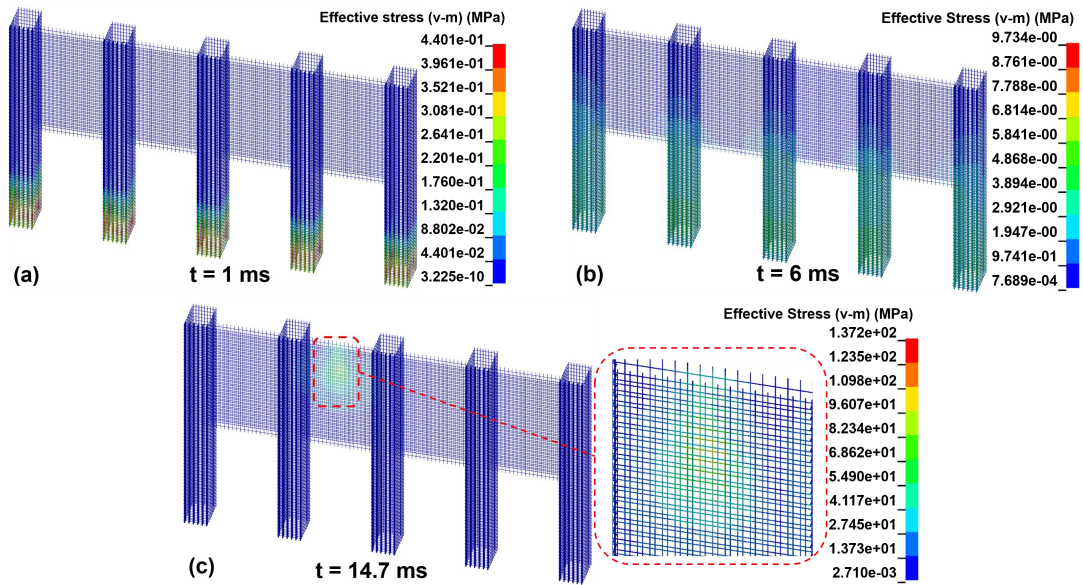


Fig. 12. Effective stress nephogram of reinforced bar under CP-V30.



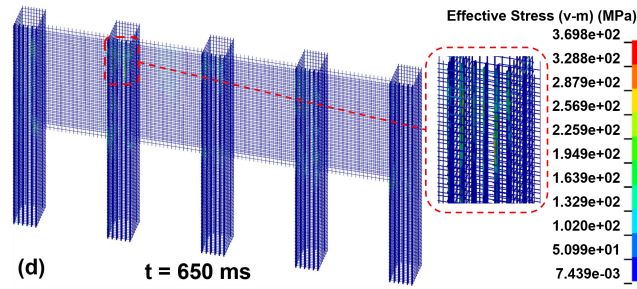


Fig. 13. Effective stress nephogram of reinforced bar under CS-V30.

248 3.1.4. Lateral displacement at the crown of different components

249 Fig. 14a presents lateral displacements at the crown of different components under CP-V30
 250 and CS-V30 conditions. The lateral displacement rapidly increased till $t = 177$ ms and gradually
 251 decreased until $t = 650$ ms. The final displacement does not reach 0, indicating plastic deformation
 252 of both the pile and the slab. Comparing the lateral displacement under CS-V30 and CP-V30 (Fig.
 253 14), the trends are consistent, but the magnitude differs. This discrepancy in magnitude can be
 254 attributed to the greater deformation capacity of slab compared to pile when subjected to the same
 255 impact energy.

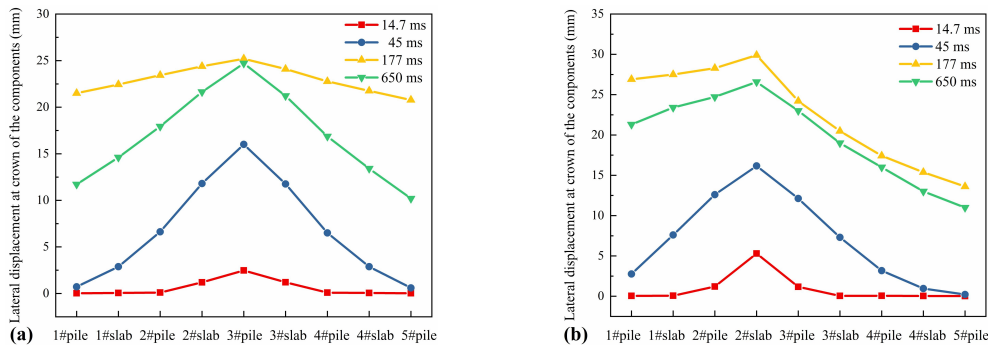


Fig. 14. Lateral displacement at crown of the components (a) CP-V30 (b) CS-V30.

256 3.1.5. Lateral displacement of piles at the ground surface

257 Fig. 15a and 16b show the dynamic curve of lateral displacement of all piles at the ground
 258 surface under CP-V30 and CS-V30, respectively. Under CP-V30, the 3# pile exhibited the
 259 maximum lateral displacement, whereas the 2# pile exhibited the maximum lateral displacement
 260 under CS-V30. This discrepancy is due to the structural asymmetry on either side of the impact
 261 center under CS-V30, which allows one side of pile #2 greater freedom, resulting in larger lateral
 262 displacement. When comparing the lateral displacement of 2# pile under CS-V30 and 3# pile
 263 under CP-V30 (Fig. 15c), it is apparent that the maximum lateral displacement of pile at the
 264 ground surface is greater under CP conditions, despite the same impact velocity. The
 265 characteristics of the lateral displacements suggest that the concrete slab is capable of undergoing

266 larger deformations and absorbing more energy.

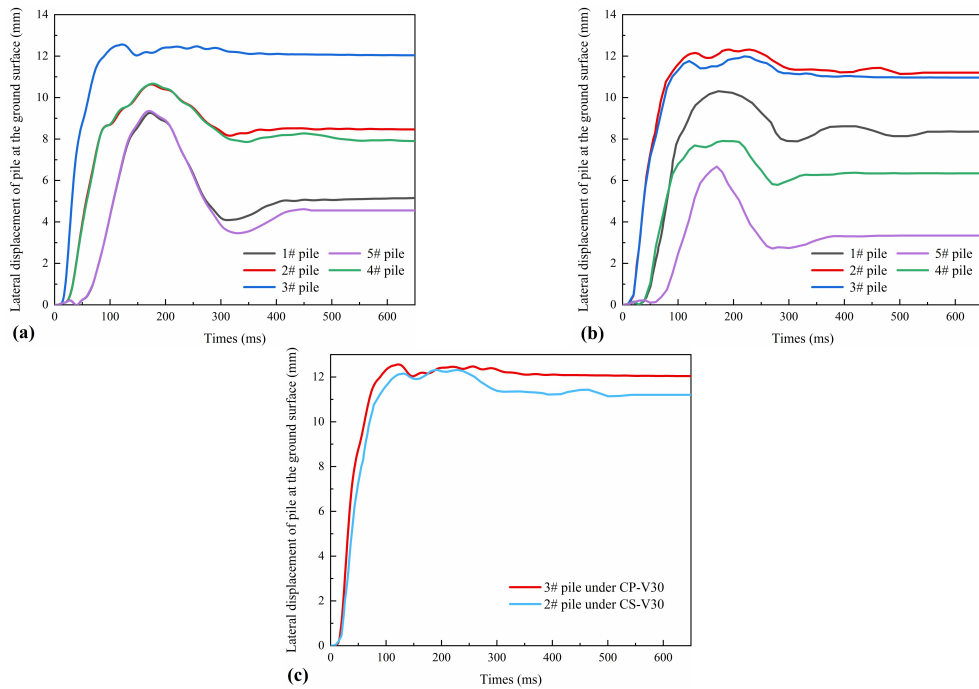
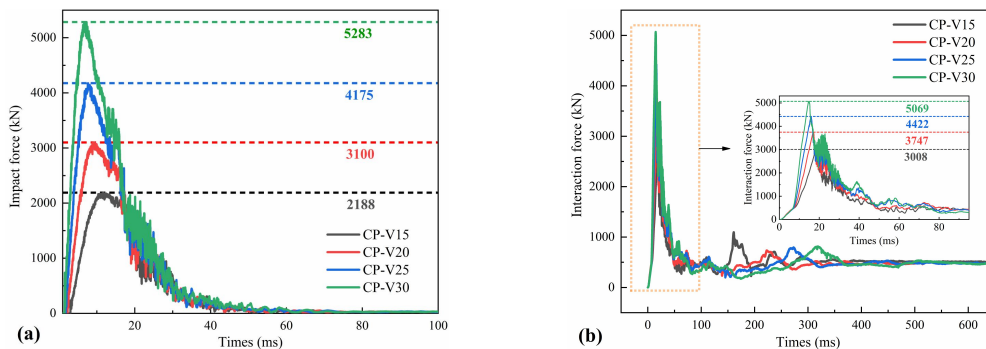


Fig. 15. Dynamic curves of lateral displacement of pile at the ground surface
 (a) CP-V30 (b) CS-V30 (c) compare between CP-V30 and CS-V30.

267 *3.2. Influence of different impact velocities*

268 Figure 17 demonstrates that under CP conditions, the impact force, interaction force, and
 269 lateral displacement of pile #3 at the ground surface increase as the impact velocity of rockfall
 270 rises. When the velocity increases from 15 m/s to 30 m/s, the impact force increases by 1.42, 1.91,
 271 and 2.41 times, the interaction force increases by 1.25, 1.47, and 1.68 times, and the lateral
 272 displacement of 3# pile at ground surface increases by 1.57, 2.24, and 3 times at $t = 650$ ms. By
 273 comparing the magnitude of changes, the lateral displacement is more sensitive to velocity
 274 variations than impact force and structural interaction force.



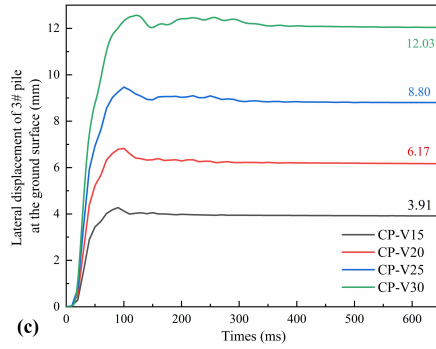


Fig. 16. Dynamic curves of evaluation indexes under various velocities

(a) impact force (b) interactional force (c) lateral displacement at the ground surface of 3# pile.

275 Fig. 17 shows the impact force, interaction force, and lateral displacement of 2# pile at the
 276 ground surface enlarge as the impact velocity increases under CS conditions. When the velocity
 277 increases from 15 m/s to 30 m/s, the impact force increases by 1.41, 1.90, and 2.41 times, the
 278 interaction force increases by 1.24, 1.47, and 1.68 times, and the lateral displacement of 3# pile at
 279 ground surface increases by 1.55, 2.23, and 3 times at $t = 650$ ms. Similar to the CP conditions, the
 280 lateral displacement is still most sensitive to velocity variations.

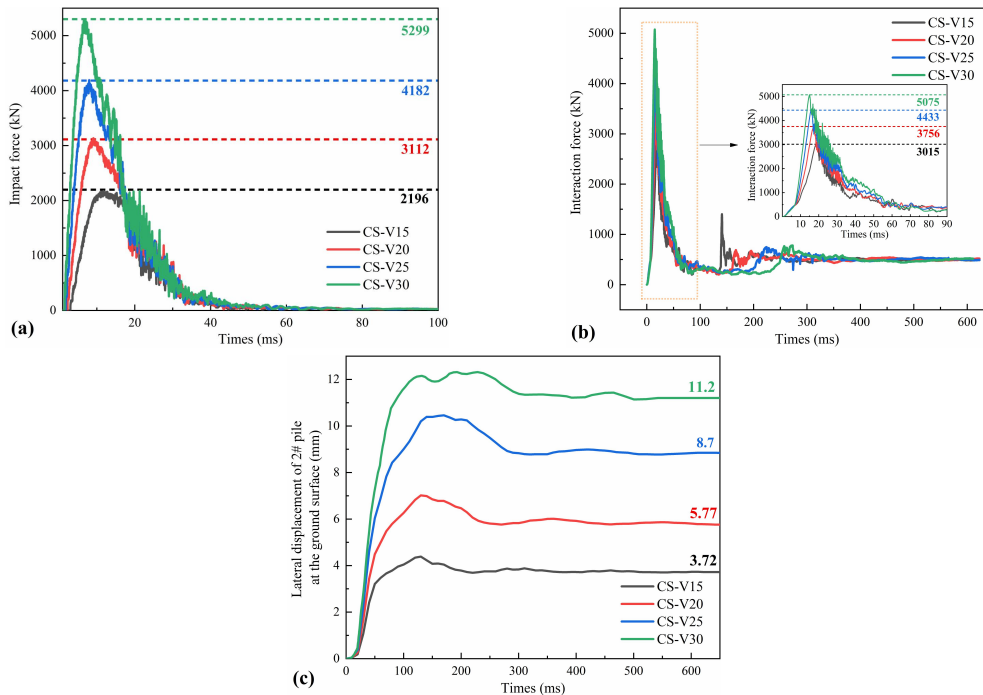


Fig. 17. Dynamic curves of evaluation indexes under various velocities

(a) impact force (b) interactional force (c) lateral displacement at the ground surface of 3# pile.

281 4. Discussions

282 4.1. Comparison of impact force calculation models

283 A comparative analysis compared the elastic theories proposed by Labiouse et al. (1996),
 284 Kawahara and Muro (2006), Pichler et al. (2006), and Hertz (1881) was conducted to assess the

285 validity of the numerical simulation (Fig. 18). The results reveal a fundamental linear correlation
 286 between impact force and velocity. Overall, the computational results are consistent with those of
 287 other models in terms of magnitude, thus confirming the validity of the calculations reported here.

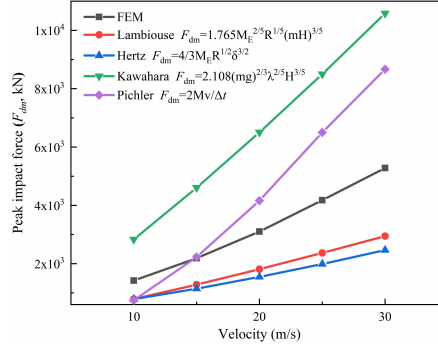


Fig. 18. Relationship between impact velocity and impact force.

288 4.2. Relationship between structural evaluation indexes and impact energy

289 Table 5 lists the initial kinetic energy of impactor (E), the peak impact force (F_{dm}), the peak
 290 interaction force (F_{im}), the ratio of the peak impact force to the peak interaction force (α), the
 291 maximum the lateral displacement of pile at the ground surface at $t = 650$ ms (S_{mpt}), the number of
 292 damage failure units (N_d), and the ratio of damage failure units to overall RC structure units (β).

293 Table 5 Simulation results of various impact cases.

Case	E (kJ)	F_{dm} (kN)	F_{im} (kN)	α (%)	S_{mpt} (mm)	N_d	β (%)
CP-V10	130	1420	2170	65.4	2.25	83	0.0059
CP-V15	292.5	2188	3008	72.7	3.91	817	0.0577
CP-V20	520	3100	3747	82.7	6.17	2179	0.1539
CP-V25	812.5	4175	4422	94.4	8.8	3088	0.2181
CP-V30	1170	5283	5069	104.2	12.03	5040	0.3559
CS-V10	130	1426	2182	65.4	1.76	52	0.0037
CS-V15	292.5	2196	3015	72.7	3.72	321	0.0227
CS-V20	520	3112	3756	82.7	5.77	1062	0.0750
CS-V25	812.5	4182	4433	94.4	8.7	2728	0.1927
CS-V30	1170	5299	5075	104.2	11.2	4880	0.3446

294 Under the premise of known impact energy, estimating impact force, interaction force, and
 295 displacement of pile for the structural design is very important. As shown in Table 5, the variation
 296 in peak impact force (F_{dm}) with different impact centers is minimal. Consequently, CP simulation
 297 results were chosen for further analysis. The dependence of the peak impact force on the impact
 298 energy is shown in Fig. 19a, with a correlation coefficient $R^2 = 0.99$, i.e.,

299
$$F_{dm} = 3.69(E + 290.33) = 1845(mv^2 + 0.58) \quad (1)$$

300 where m is the impactor mass ($m = 2600$ kg herein); v is the initial impact velocity (10 m/s \leq
 301 $v \leq 30$ m/s herein).

302 The dependence of the ratio of peak impact force to peak interaction force on the impact
 303 energy is shown in Fig. 19b, with a correlation coefficient of 0.99, i.e.,

304
$$\alpha = 0.037(E + 1671.89) = 18.5(mv^2 + 3.34) \quad (2)$$

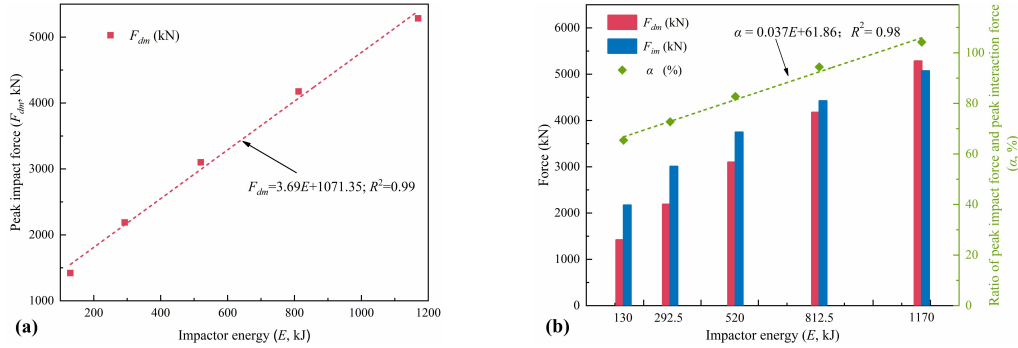


Fig. 19. Dependence of various indexes on impactor energy (a) peak impact force (b) the ratio of peak impact force and peak interaction force.

305 The lateral displacement of pile at the ground surface is an important index to judge the
 306 failure of pile foundation under lateral load. As shown in Table 5, the maximum lateral
 307 displacement of pile at the ground surface under pile as impact center is greater than that under
 308 slab as impact center. Therefore, the situation where the pile is the center of impact is the more
 309 dangerous. As shown in Fig. 20, with the increase of impact energy, the displacement value and
 310 number of damage failure units enlarges, which means the structure suffers more damage under
 311 CP. Furthermore, the maximum lateral displacement of pile at the ground surface when t = 650 ms,
 312 can be calculated by the following equation:

313
$$S_{mpt} = 0.00934(E + 164.88) = 4.67(mv^2 + 0.33) \quad (3)$$

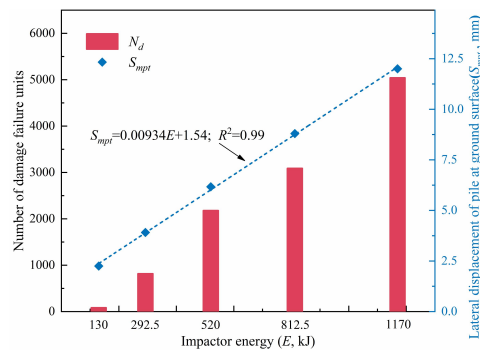


Fig. 20. Dependence of the lateral displacement of 3# pile at the ground surface on impactor energy

314 According to the Chinese Specification for the Design of Rock Retaining Wall Engineering in
 315 Geological Hazards (CAGHP, 2019), the lateral displacement of the resistant sliding pile at the
 316 ground surface must not exceed 10 mm. Substituting this value into Formula 3, the maximum

317 impact energy that the PSRW can withstand in this study is 905 kJ.

318 4.3. Comparison with other concrete rockfall retaining walls

319 Table 6 presents crucial data on an improved cast-in-place rockfall concrete barrier developed
320 by the US Department of Transportation (Patnaik et al., 2015). This barrier exhibits relatively low
321 resistance to impact energy, which restricts its applicability to situations where high-impact energy
322 rockfalls are likely to occur. Integrating a specialized buffering layer on the concrete retaining wall,
323 the barrier's impact resistance can be effectively enhanced (Kurihashi et al., 2020). According to
324 Maegawa et al. (2011), concrete rockfall barriers with a buffering layer offer a maximum impact
325 resistance ranging from approximately 120 to 490 kJ. Addressing the resistance limitations of
326 traditional concrete rockfall barriers, Furet et al. (2022) proposed the articulated concrete block
327 rockfall protection structures. These innovative structures allow concrete blocks hingedly
328 connected to one another, enabling greater impact energy absorption.

329 **Table 6** Comparison of different concrete rockfall protection structures

Structure name	The maximum impact energy that structure can withstand (kJ)	Energy dissipation ratio (%)	Interception altitude (m)
Cast-in-place rockfall concrete barriers (Patnaik et al., 2015)	127	/	0.81
Concrete retaining wall with buffering system (Kurihashi et al., 2020)	273	100	2.5
Concrete rock – wall (Maegawa et al., 2011)	490	/	/
Articulated concrete blocks rockfall protection structure (Furet et al., 2022)	1020	100	3.2
Pile-slab retaining wall	905	100	6

330 Note: Energy dissipation ratio denotes the ratio of dissipated energy to input energy.

331 In terms of energy dissipation, structure damage and friction are responsible for 74% of the
332 impact energy dissipation, with the remaining 26% attributed to other phenomena such as
333 deformation of structural elements, elastic wave propagation, viscous damping, and fracturing.
334 Compared to conventional concrete rockfall barriers, PSRW exhibit significantly higher impact
335 resistance (905 kJ) and interception height (6 m). Similarly, these structures absorb all the impact
336 energy, preventing the impactor from rebounding.

337 For traditional RC retaining walls subjected to a 16 kJ impact energy, shear cracks develop
338 diagonally from the impact point, with wider spreading observed on the rear face compared to the
339 collision surface (Kurihashi et al., 2020). Fig. 21 illustrates the concrete damage nephogram of

340 PSRW under the impact load of 1170 kN. It is evident that concrete damage primarily
 341 concentrated around the impact point and at the junction between the pile and slab. Importantly,
 342 there is no evidence of crack penetration into the structure itself, indicating that the PSRW
 343 maintains its structural integrity.

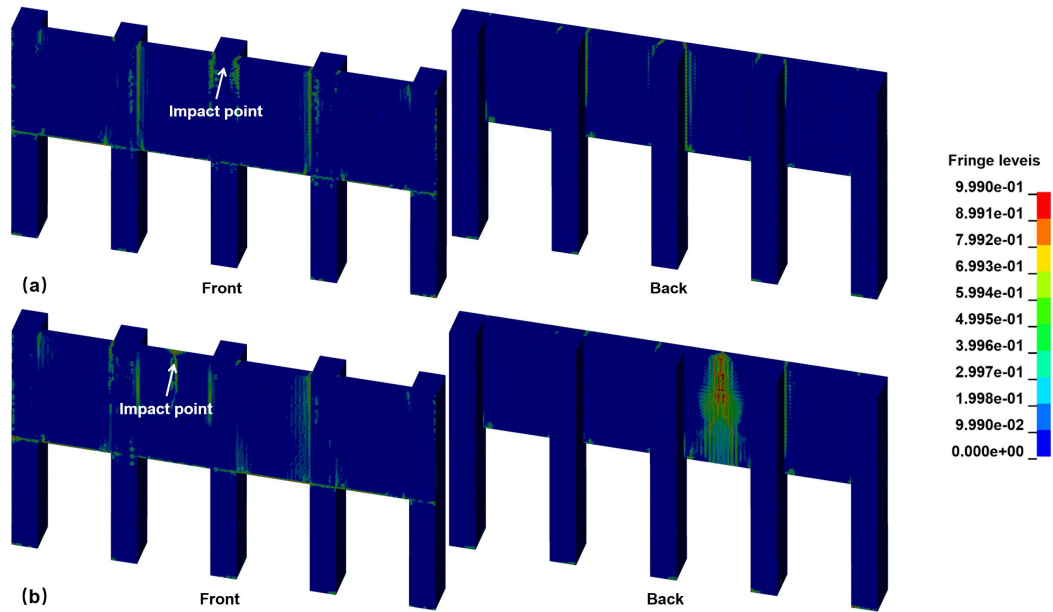


Fig. 21. Damage nephogram of concrete at $t = 650$ ms (a) CP-V30 (b) CS-V30.

344 Although the lateral displacement of the pile exceeds the stipulated limit, reaching 12 mm as
 345 indicated in Table 5 and Figure 21, it is essential to acknowledge that the specified ultimate lateral
 346 displacement is frequently a conservative estimation. Concurrently, the maximum lateral
 347 displacement at the crown of the cantilever section is 35 mm, which is substantially less than the
 348 lateral displacement threshold for the cantilever section of the anti-slide pile. This threshold is
 349 defined as 1% of the cantilever section's length, according to CAGHP (2019). As a result, the
 350 impact load does not compromise the integrity of the structure.

351 In summary, the PSRW is an innovative rockfall protection structure, providing an enhanced
 352 level of impact resistance, increased interception height, and reduced concrete damage.
 353 Additionally, the minimal lateral displacement observed after impact further ensures the structural
 354 integrity and safety in challenging terrain areas.

355 4.4. Discussion on Engineering Practicality

356 The data presented in Table 7 reveal the distribution of rockfall energy levels across four
 357 regions that experience frequent rockfalls. Notably, the Alps region experiences substantial
 358 rockfalls, with many of them exhibiting an impact energy below 1000 kJ. Schneider et al. (2023)

359 utilized Doppler radar technology to monitor rockfall activity in Brienz/Brinzals, Switzerland.
 360 Their findings indicated that although the volume of rockfalls ranged from 1 to 100 m³, smaller
 361 events (1 m³) were markedly more common. As previously mentioned, the PSRW can withstand
 362 rockfalls with an impact energy of about 1000 kJ, making it an ideal solution for a multitude of
 363 small alpine rockfall scenarios. Additionally, its compact size and robust structural stability further
 364 enhance its suitability for mountainous construction projects. In cases where the impact energy of
 365 falling rocks exceeds 1000 kJ, it is advisable to optimize the mechanical properties of the cushion
 366 layer, improve the elastic modulus of concrete, increase the reinforcement ratio of longitudinal
 367 tension bars, enlarge the section size of pile at ground level, or add anchoring measures to enhance
 368 the bending resistance of the retaining structure.

369 **Table 7** Rockfall events in different areas

Study area	Total number of rockfall events	Rockfall energy < 1000 kJ	Percentage
French Alps (Le Roy et al., 2019)	18	9	50%
Swiss Alps (Dietze et al., 2017)	37	37	100%
Along the railway in Japan (Muraishi et al., 2005)	173	158	91%
New South Wales, Australia (Spadari et al., 2013)	211	200	94%

370 **5. Conclusion**

371 Compared to existing rockfall protection structures, the PSRW offers enhanced stability and
 372 requires a smaller footprint, making it adept at addressing a broad spectrum of rockfall impact
 373 scenarios commonly encountered in alpine canyon regions. In this paper, the dynamic response of
 374 the PSRW under different impact centers and velocities were compared and analyzed using the
 375 FEM simulation method. Additionally, the influencing factors such as peak impact force, peak
 376 interaction force, ratio of peak impact force to peak interaction force, concrete stress,
 377 reinforcement stress, maximum lateral displacement of the pile at the ground surface, and ratio of
 378 damage failure units to overall structure units were quantified. Notably, the formula for calculating
 379 the peak impact force of the PSRW (Eqs. 1), the ratio of peak impact force to peak interaction
 380 force (Eqs. 2), maximum lateral displacement of the pile at the ground surface (Eqs. 3) based on
 381 the impact energy of rockfalls were proposed. The key findings of this study are as follows:

382 (1) The impact force, interaction force and lateral displacement exhibit a linear correlation
 383 with the impact velocity. however, the lateral displacement is more sensitive to velocity variations

384 than the impact force and interaction force.

385 (2) Under different impact centers, the variations in impact force and interaction force are
386 minimal. When the pile serves as the impact center, the lateral displacement of pile at the ground
387 surface and the extent of concrete damage are significantly greater than when the slab center is the
388 impact center. This indicates that impacts centered on the pile pose a more hazardous impact
389 scenario.

390 (3) Concrete damage predominantly concentrates at the joints between piles and slabs, the
391 impact center itself, and the section of piles at the ground surface. To minimize structural concrete
392 damage, it is imperative to prioritize these critical sections in the structural design.

393 (4) The impact force, the ratio of peak impact force to peak interaction force, and the
394 maximum lateral displacement of the pile at the ground surface have a significant correlation with
395 the impact energy. These relationships are crucial for evaluating impact force, interaction force,
396 and the lateral displacement of piles at ground surface during the design of PRSW structures.
397 According to Chinese specifications for displacement requirements, the maximum lateral
398 displacement of the pile at the ground surface should not exceed 10 mm. Consequently, the
399 maximum impact energy that the PSRW can withstand is 905 kJ, when the crown is designated as
400 the impact center.

401 **CRedit authorship contribution statement**

402 **Peng Zou:** Methodology, Simulation, Visualization, Writing - original draft. **Gang Luo:**
403 Tests design, funding acquisition, writing - review. **Yuzhang Bi:** Visualization, Writing - review.
404 **Hanhua Xu:** Writing - review.

405 **Declaration of Competing Interest**

406 The authors declare that they have no known competing financial interests or personal
407 relationships that could have appeared to influence the work reported in this paper.

408 **Acknowledgments**

409 This research was funded by the National Natural Science Foundation of China (42277143),
410 the National Key R&D Program of China (2022YFC3005704), the Sichuan Province Science and
411 Technology Support Program (2024NSFSC0100) and the Science and the research project of the

412 Department of Natural Resources of Sichuan Province (KJ-2023-004, KJ-2023-029). The authors
413 also thank the editors and anonymous reviewers for their constructive comments that improved the
414 manuscript.

415 **References**

- 416 Bhatti, A. Q. and Kishi, N.: Impact response of RC rock-shed girder with sand cushion under falling
417 load, *Nuclear Engineering and Design*, 240, 2626-2632,
418 <https://doi.org/10.1016/j.nucengdes.2010.07.029>, 2010.
- 419 Bi, Y., Li, M., Wang, D., Zheng, L., Yan, S., and He, S.: A numerical study of viscous granular flow in
420 artificial step-pool systems: flow characteristics and structure optimization, *Acta Geotechnica*,
421 <https://doi.org/10.1007/s11440-023-01933-1>, 2023.
- 422 CAGHP: Code for design of rock retaining wall engineering in geological hazards (T/CAGHP060-
423 2019), China University of Geosciences Press, Wuhan2019. (in Chinese)
- 424 Chau, K. T., Wong, R., and Wu, J.: Coefficient of restitution and rotational motions of rockfall impacts,
425 *International Journal of Rock Mechanics and Mining Sciences*, 39, 69-77,
426 [https://doi.org/10.1016/S1365-1609\(02\)00016-3](https://doi.org/10.1016/S1365-1609(02)00016-3), 2002.
- 427 Crosta, G. and Agliardi, F.: Parametric evaluation of 3D dispersion of rockfall trajectories, *Natural
428 Hazards and Earth System Sciences*, 4, 583-598, <https://doi.org/10.5194/nhess-4-583-2004>, 2004.
- 429 Demartino, C., Wu, J. G., and Xiao, Y.: Response of shear-deficient reinforced circular RC columns
430 under lateral impact loading, *International Journal of Impact Engineering*, 109, 196-213,
431 <https://doi.org/10.1016/j.ijimpeng.2017.06.011>, 2017.
- 432 Dietze, M., Mohadjer, S., Turowski, J. M., Ehlers, T. A., and Hovius, N. J. E. S. D.: Seismic monitoring
433 of small alpine rockfalls—validity, precision and limitations, 5, 653-668, 2017.
- 434 Fan, W., Zhong, Z., Huang, X., Sun, W., and Mao, W.: Multi-platform simulation of reinforced concrete
435 structures under impact loading, *Engineering Structures*, 266, 114523,
436 <https://doi.org/10.1016/j.engstruct.2022.114523>, 2022.
- 437 Furet, A., Villard, P., Jarrin, J.-P., and Lambert, S.: Experimental and numerical impact responses of an
438 innovative rockfall protection structure made of articulated concrete blocks, *Rock Mechanics and
439 Rock Engineering*, 55, 5983-6000, <https://doi.org/10.1007/s00603-022-02957-x>, 2022.
- 440 Heng, K., Li, R., Li, Z., and Wu, H.: Dynamic responses of highway bridge subjected to heavy truck
441 impact, *Engineering Structures*, 232, 11828-11850,
442 <https://doi.org/10.1016/j.engstruct.2020.111828>, 2021.
- 443 Hertz, H.: The contact of elastic solids, *J Reine Angew, Math*, 92, 156-171, 1881.
- 444 Hu, X., Mei, X., Yang, Y., and Luo, G.: Dynamic Response of Pile-plate Rock Retaining Wall under
445 Impact of Rockfall, *Journal of Engineering Geology*, 27, 123-133, 2019. (in Chinese)
- 446 Hungr, O., Leroueil, S., and Picarelli, L.: The Varnes classification of landslide types, an update,
447 *Landslides*, 11, 167-194, <https://doi.org/10.1007/s10346-013-0436-y>, 2014.
- 448 Kawahara, S. and Muro, T.: Effects of dry density and thickness of sandy soil on impact response due
449 to rockfall, *Journal of terramechanics*, 43, 329-340, <https://doi.org/10.1016/j.jterra.2005.05.009>,
450 2006.
- 451 Kurihashi, Y., Oyama, R., Komuro, M., Murata, Y., and Watanabe, S.: Experimental study on buffering
452 system for concrete retaining walls using geocell filled with single-grain crushed stone,
453 *International Journal of Civil Engineering*, 18, 1097-1111, <https://doi.org/10.1007/s40999-020-00520-9>, 2020.
- 454
455 Labiouse, V., Descoedres, F., and Montani, S.: Experimental study of rock sheds impacted by rock
456 blocks, *Structural Engineering International*, 6, 171-176,
457 <https://doi.org/10.2749/101686696780495536>, 1996.

458 Lambert, S., Gotteland, P., and Nicot, F.: Experimental study of the impact response of geocells as
459 components of rockfall protection embankments, *Natural Hazards and Earth System Sciences*, 9,
460 459-467, <https://doi.org/10.5194/nhess-9-459-2009>, 2009.

461 Le Roy, G., Helmstetter, A., Amitrano, D., Guyoton, F., and Le Roux-Mallouf, R.: Seismic analysis of
462 the detachment and impact phases of a rockfall and application for estimating rockfall volume and
463 free-fall height, 124, 2602-2622, <https://doi.org/10.1029/2019JF004999>, 2019.

464 Lee, K., Chang, N., and Ko, H.: Numerical simulation of geosynthetic-reinforced soil walls under
465 seismic shaking, *Geotextiles and Geomembranes*, 28, 317-334,
466 <https://doi.org/10.1016/j.geotextmem.2009.09.008>, 2010.

467 Lu, L., Lin, H., Wang, Z., Xiao, L., Ma, S., and Arai, K.: Experimental and numerical investigations of
468 reinforced soil wall subjected to impact loading, *Rock Mechanics and Rock Engineering*, 54,
469 5651-5666, <https://doi.org/10.1007/s00603-021-02579-9>, 2021.

470 Maegawa, K., Yokota, T., and Van, P. T.: Experiments on rockfall protection embankments with
471 geogrids and cushions, *GEOMATE Journal*, 1, 19-24, 2011.

472 Mavrouli, O., Giannopoulos, P., Carbonell, J. M., and Syrmakizis, C.: Damage analysis of masonry
473 structures subjected to rockfalls, *Landslides*, 14, 891-904, [https://doi.org/10.1007/s10346-016-](https://doi.org/10.1007/s10346-016-0765-8)
474 [0765-8](https://doi.org/10.1007/s10346-016-0765-8), 2017.

475 Muraishi, H., Samizo, M., and Sugiyama, T.: Development of a flexible low-energy rockfall protection
476 fence, *Quarterly Report of RTRI*, 46, 161-166, <https://doi.org/10.2219/rtriqr.46.161>, 2005.

477 Patnaik, A., Musa, A., Marchetty, S., and Liang, R.: Full-scale testing and performance evaluation of
478 rockfall concrete barriers, *Transportation research record*, 2522, 27-36,
479 <https://doi.org/10.3141/2522-03>, 2015.

480 Peila, D. and Ronco, C.: Design of rockfall net fences and the new ETAG 027 European guideline,
481 *Natural Hazards and Earth System Sciences*, 9, 1291-1298, [https://doi.org/10.5194/nhess-9-1291-](https://doi.org/10.5194/nhess-9-1291-2009)
482 [2009](https://doi.org/10.5194/nhess-9-1291-2009), 2009.

483 Peila, D., Oggeri, C., and Castiglia, C.: Ground reinforced embankments for rockfall protection: design
484 and evaluation of full scale tests, *Landslides*, 4, 255-265, [https://doi.org/10.1007/s10346-007-](https://doi.org/10.1007/s10346-007-0081-4)
485 [0081-4](https://doi.org/10.1007/s10346-007-0081-4), 2007.

486 Perera, J. S., Lam, N., Disfani, M. M., and Gad, E.: Experimental and analytical investigation of a RC
487 wall with a gabion cushion subjected to boulder impact, *International Journal of Impact*
488 *Engineering*, 151, 103823-103839, <https://doi.org/10.1016/j.ijimpeng.2021.103823>, 2021.

489 Pichler, B., Hellmich, C., Mang, H. A., and Eberhardsteiner, J.: Loading of a gravel-buried steel pipe
490 subjected to rockfall, *Journal of Geotechnical and Geoenvironmental Engineering*, 132, 1465-
491 1473, [https://doi.org/10.1061/\(ASCE\)1090-0241\(2006\)132:11\(1465\)](https://doi.org/10.1061/(ASCE)1090-0241(2006)132:11(1465)), 2006.

492 Schellenberg, K.: On the design of rockfall protection galleries, ETH Zurich, 2008.

493 Schneider, M., Oestreicher, N., Ehrat, T., and Loew, S.: Rockfall monitoring with a Doppler radar on an
494 active rockslide complex in Brienz/Brinzauls (Switzerland), 23, 3337-3354,
495 <https://doi.org/10.5194/nhess-23-3337-2023>, 2023.

496 Shen, W., Zhao, T., Dai, F., Jiang, M., and Zhou, G. G.: DEM analyses of rock block shape effect on
497 the response of rockfall impact against a soil buffering layer, *Engineering Geology*, 249, 60-70,
498 <https://doi.org/10.1016/j.enggeo.2018.12.011>, 2019.

499 Spadari, M., Kardani, M., De Carteret, R., Giacomini, A., Buzzi, O., Fityus, S., and Sloan, S.:
500 Statistical evaluation of rockfall energy ranges for different geological settings of New South
501 Wales, Australia, 158, 57-65, <https://doi.org/10.1016/j.enggeo.2013.03.007>, 2013.

502 Truong, P. and Lehane, B.: Effects of pile shape and pile end condition on the lateral response of
503 displacement piles in soft clay, *Géotechnique*, 68, 794-804, <https://doi.org/10.1680/jgeot.16.P.291>,
504 2018.

505 Volkwein, A., Schellenberg, K., Labiouse, V., Agliardi, F., Berger, F., Bourrier, F., Dorren, L. K., Gerber,
506 W., and Jaboyedoff, M.: Rockfall characterisation and structural protection—a review, *Natural*
507 *Hazards and Earth System Sciences*, 11, 2617-2651, <https://doi.org/10.5194/nhess-11-2617-2011>,
508 2011.

509 Wu, J., Ma, G., Zhou, Z., Mei, X., and Hu, X.: Experimental Investigation of Impact Response of RC
510 Slabs with a Sandy Soil Cushion Layer, *Advances in Civil Engineering*, 2021, 1-18,
511 <https://doi.org/10.1155/2021/1562158>, 2021.

512 Yang, J., Duan, S., Li, Q., and Liu, C.: A review of flexible protection in rockfall protection, *Natural*
513 *Hazards*, 99, 71-89, <https://doi.org/10.1007/s11069-019-03709-x>, 2019.

514 Yong, A. C., Lam, N. T., and Menegon, S. J.: Closed-form expressions for improved impact resistant
515 design of reinforced concrete beams, *Structures*, 29, 1828-1836,
516 <https://doi.org/10.1016/j.istruc.2020.12.041>, 2021.

517 Yong, A. C., Lam, N. T., Menegon, S. J., and Gad, E. F.: Experimental and analytical assessment of
518 flexural behavior of cantilevered RC walls subjected to impact actions, *Journal of Structural*
519 *Engineering*, 146, 04020034, [https://doi.org/10.1061/\(ASCE\)ST.1943-541X.0002578](https://doi.org/10.1061/(ASCE)ST.1943-541X.0002578), 2020.

520 Yu, Z., Luo, L., Liu, C., Guo, L., Qi, X., and Zhao, L.: Dynamic response of flexible rockfall barriers
521 with different block shapes, *Landslides*, 18, 2621-2637, [https://doi.org/10.1007/s10346-021-](https://doi.org/10.1007/s10346-021-01658-w)
522 [01658-w](https://doi.org/10.1007/s10346-021-01658-w), 2021.

523 Zhao, P., Xie, L., Li, L., Liu, Q., and Yuan, S.: Large-scale rockfall impact experiments on a RC rock-
524 shed with a newly proposed cushion layer composed of sand and EPE, *Engineering Structures*,
525 175, 386-398, <https://doi.org/10.1016/j.engstruct.2018.08.046>, 2018.

526 Zhong, H., Lyu, L., Yu, Z., and Liu, C.: Study on mechanical behavior of rockfall impacts on a shed
527 slab based on experiment and SPH-FEM coupled method, *Structures*, 33, 1283-1298,
528 <https://doi.org/10.1016/j.istruc.2021.05.021>, 2021.

529 Zhong, H., Yu, Z., Zhang, C., Lyu, L., and Zhao, L.: Dynamic mechanical responses of reinforced
530 concrete pier to debris avalanche impact based on the DEM-FEM coupled method, *International*
531 *Journal of Impact Engineering*, 167, 104282-104301,
532 <https://doi.org/10.1016/j.ijimpeng.2022.104282>, 2022.